Indistinguishability domains of neural microcircuit motifs mapped through classification scores of postsynaptic spike counts

Anjali Naveen Kumar
Tata Institute of Fundamental Research Hyderabad
Hyderabad 500046, India
anjali@tifrh.res.in

Raghunathan Ramakrishnan
Tata Institute of Fundamental Research Hyderabad
Hyderabad 500046, India
ramakrishnan@tifrh.res.in

Abstract

In the kinetic modeling of a chemical synapse, the reversal potential (E_{syn}) and conductance amplitude ($\overline{g}_{\text{syn}}$) of the synapse jointly regulate the spike-induced activity of the postsynaptic neuron. We simulate two-neuron microcircuit motifs of feedforward ($i \rightarrow j$) and feedback ($i \rightleftharpoons j$) types using random external current pulses provided only at the presynaptic neuron. For combinations of E_{syn} and $\overline{g}_{\text{syn}}$, corresponding to an excitatory synapse, a supervised machine learning method for classification distinguishes the motifs perfectly with a score of 1.0 when using binned counts of postsynaptic spikes as the input. Strongly inhibitory combinations of these parameters result in no postsynaptic response in both types of microcircuit motifs; hence, the classifier does not improve upon a random assignment with a score of 0.5. In other domains of the parameter space spanned by E_{syn} and $\overline{g}_{\text{syn}}$, corresponding to diminished excitation/inhibition, the classifier fails ($0.5 < \text{score} < 1$), indicating the challenge in identifying the nature of the synapse inferred exclusively from postsynaptic spikes. For this task, the gradient boosting classifier gives higher classification accuracies that improve with further training, compared to other classifiers explored in this study.

Keywords

Neural circuits, Chemical synapse, Action potentials, Machine learning, Network classification

ACM Reference Format:
Anjali Naveen Kumar and Raghunathan Ramakrishnan. 2025. Indistinguishability domains of neural microcircuit motifs mapped through classification scores of postsynaptic spike counts . In *Proceedings of (Preprint).*

1 Introduction

The human brain comprises a highly complex yet coordinated network of over 10 billion neurons [1]. Neurons possess the unique ability to conduct electrical signals through the generation of action potentials, forming the foundation of neural communication. Synapses serve as the junctions between neurons, enabling this communication. Upon stimulation, the presynaptic neuron releases neurotransmitters, which can lead to either excitation or inhibition of the postsynaptic neuron, depending on the type of neurotransmitter molecules (e.g., glutamate, Glu, for excitation and γ-aminobutyric acid, GABA, for inhibition). These neurotransmitters bind to specific receptors on the postsynaptic neuronal membrane, producing a transient shift in the resting membrane potential (V_{rest}). This change manifests as either an excitatory postsynaptic potential (EPSP) or an inhibitory postsynaptic potential (IPSP), determined by the type of ion channel activated [2]. EPSPs arise when Glu receptors open [3], allowing Na^+ and Ca^{2+} ions to enter the cell. This influx drives the synaptic reversal potential (E_{syn}) toward ~0 mV, resulting in depolarization [4]. In contrast, activation of postsynaptic ionotropic $GABA_A$ receptors permits Cl^- influx in mature neurons, shifting E_{syn} toward approximately −70 mV [5], thereby producing hyperpolarization [6, 7]. In general, if E_{syn} lies below V_{rest}, the postsynaptic effect is inhibitory; conversely, if E_{syn} exceeds V_{rest}, the effect is excitatory [8].

The electrical activity of the neuronal membrane determines the impact of synaptic input currents. The driving force of a synaptic current is given by the difference between V_{rest} and E_{syn} [9]. As current flows, the membrane potential shifts toward E_{syn}, gradually reducing the driving force. Thus, EPSPs from active synapses do not simply add linearly [9]. Moreover, an increase in synaptic conductance lowers the membrane resistance, which reduces the amplitude and accelerates the decay of EPSPs [9]. Neurotransmitters mediate communication between presynaptic and postsynaptic neurons. Excitatory neurotransmitters, glutamate, act on AMPA/kainate and NMDA receptors, both with reversal potentials near 0 mV. Inhibitory GABAergic synapses act primarily via $GABA_A$ receptors ($E_{\text{syn}} \approx -70$ mV) , with $GABA_B$ receptors operating at even more hyperpolarized levels ($E_{\text{syn}} \approx -95$ mV) [10, 11]. The exact value of the reversal potential is not fixed but depends on developmental, spatial, and microenvironmental factors. For instance, in immature neurons, intracellular Cl^- concentration is higher due to the activity of the Na–K–2Cl cotransporter (NKCC) [12]. As a result, activation of $GABA_A$ receptors produces depolarization rather than hyperpolarization [7]. With a resting potential of around −75 mV, the opening of relatively few $GABA_A$ channels can generate large depolarizations in immature neurons due to their high input resistance [12]. Additionally, GABA can reduce excitatory glutamatergic EPSPs through shunting inhibition, the extent of which depends on the density of glutamatergic inputs [12]. During development, this balance shifts: GABAergic transmission transitions from excitatory to inhibitory as chloride homeostasis matures and shunting inhibition becomes dominant [11].

At later stages of development, upregulation of the K–Cl cotransporter isoform 2 (KCC2) drives Cl^- efflux, which reverses the transmembrane Cl^- gradient and shifts the sign of E_{syn}. Consequently, activation of the GABA receptor results in influx of Cl^-, thereby establishing the inhibitory action of GABA [13]. In vitro studies indicate that this upregulation is promoted by "miniature postsynaptic currents", which occur independently of action potentials. These depolarizations trigger Ca^{2+} signaling, which in turn enhances the expression of the K-Cl co-transporter, KCC2 [12, 14].

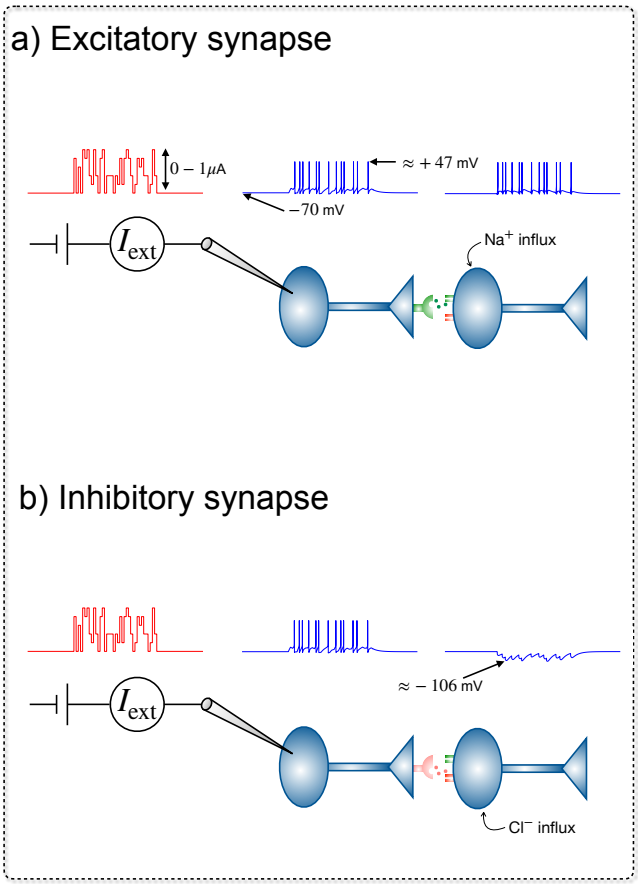

Figure 1: Schematic of excitatory and inhibitory synaptic transmission with identical peak conductance ($\overline{g}_{syn}$ = 0.2 mS/cm^2): a) Release of neurotransmitters (e.g. glutamate) leading to opening of postsynaptic receptors (ion channels), allowing Na$^+$ influx and depolarization toward the excitatory reversal potential (E_{syn} = −30 mV); b) Release of neurotransmitters (e.g. GABA) activating ion channels that allow Cl$^-$ influx in the postsynaptic neuron and hyperpolarization toward the inhibitory reversal potential (E_{syn} = −80 mV).

This developmental "GABA shift", together with the maturation of glutamatergic neurons, synapse formation, and experience-driven pruning, shapes a synchronized neuronal network [15]. Balanced excitatory and inhibitory inputs at distinct spatial domains ensure plasticity, synchrony, and proper brain oscillations. For instance, exogenous application of GABA has been shown to inhibit action potentials in pyramidal neurons when applied at the soma but to produce depolarization when applied near dendrites [16]. In hippocampal CA1 pyramidal neurons, GABA can also evoke a biphasic response: an initial hyperpolarization followed by slow depolarization [17]. GABAergic interneurons play central roles in establishing inhibitory circuits essential for orchestrating complex network activity. Disruptions in their development can contribute to neurodevelopmental disorders[18]. For example, in schizophrenia, expression of GAD67, the enzyme converting glutamate to GABA, is reduced in parvalbumin-positive (PV$^+$) interneurons, impairing gamma oscillations in the cortex and hippocampus, weakening inhibitory function [19, 20]. Similarly, loss of hippocampal GABAergic interneurons reduces inhibitory control over principal cells, facilitating hyperexcitability and seizure spread in epilepsy [21].

Excitatory and inhibitory synapses are classical paradigms of neuronal communication. Yet, in more complex contexts—such as brain development, where GABAergic transmission initially acts excitatory before shifting to inhibitory, or in epilepsy, where disrupted excitation–inhibition balance drives seizures, this dichotomy becomes less distinct. In this paper, we aim to construct a conceptual map of synaptic behavior in the parameter space defined by E_{syn} and $\overline{g}_{syn}$. By simulating prototypical cortical fast-spiking microcircuit motifs and quantifying synaptic effects using a classification score from a supervised machine learning (ML) method, we identify regions that correspond to distinct synaptic regimes.

This paper is organized as follows. In Section 2, we introduce the mathematical models used to simulate current-pulse stimulation on neural microcircuit motifs and describe the two motifs analyzed in this work. Section 3 presents the classification results, where binned spike counts of postsynaptic neurons are used as features across different values of E_{syn} and $\overline{g}_{syn}$, capturing excitatory, inhibitory, and intermediate synaptic regimes with reduced polarity. We examine the performance of machine learning methods, including improvements in classification scores with increasing training set size, and assess the tradeoff between information content and noise when spike counts are binned at different temporal resolutions. We then identify regions of the parameter space that are classifiable in a data-driven manner, as well as indistinguishable regions where classification fails and intermediate scores emerge. Finally, we conclude by outlining the broader scope of this framework for identifying neural microcircuit motifs.

2 Kinetic Modeling of Neuronal Membrane Potential

We simulate the current-pulse dynamics of microcircuit motifs consisting of two neurons, i and j, connected via a synaptic contact, as illustrated in Figure 1. The dynamics of this coupled system is described by an eight-dimensional Hodgkin–Huxley-type model:

$$\frac{d}{dt}\mathbf{y}(t) = \mathbf{f}(\mathbf{y}(t)), \tag{1}$$

where

$$\mathbf{y}(t) = \left[V_i(t), m_i(t), h_i(t), n_i(t), V_j(t), m_j(t), h_j(t), n_j(t)\right]. \tag{2}$$

Here, $V(t)$ denotes the membrane potential, and $m(t)$, $h(t)$, and $n(t)$ represent the gating variables. Each component of

$$\mathbf{f}(t) = \left[f_1(t), \ldots, f_8(t)\right] \tag{3}$$

specifies the corresponding differential equation governing one of the eight dynamical variables.

The membrane potential of the presynaptic neuron (i) is modeled using the Hodgkin–Huxley framework [22–25]:

$$C_m \frac{dV_i}{dt} = I_{ext}(t) - I_{Na,i}(t) - I_{K,i}(t) - I_{leak,i}(t), \tag{4}$$

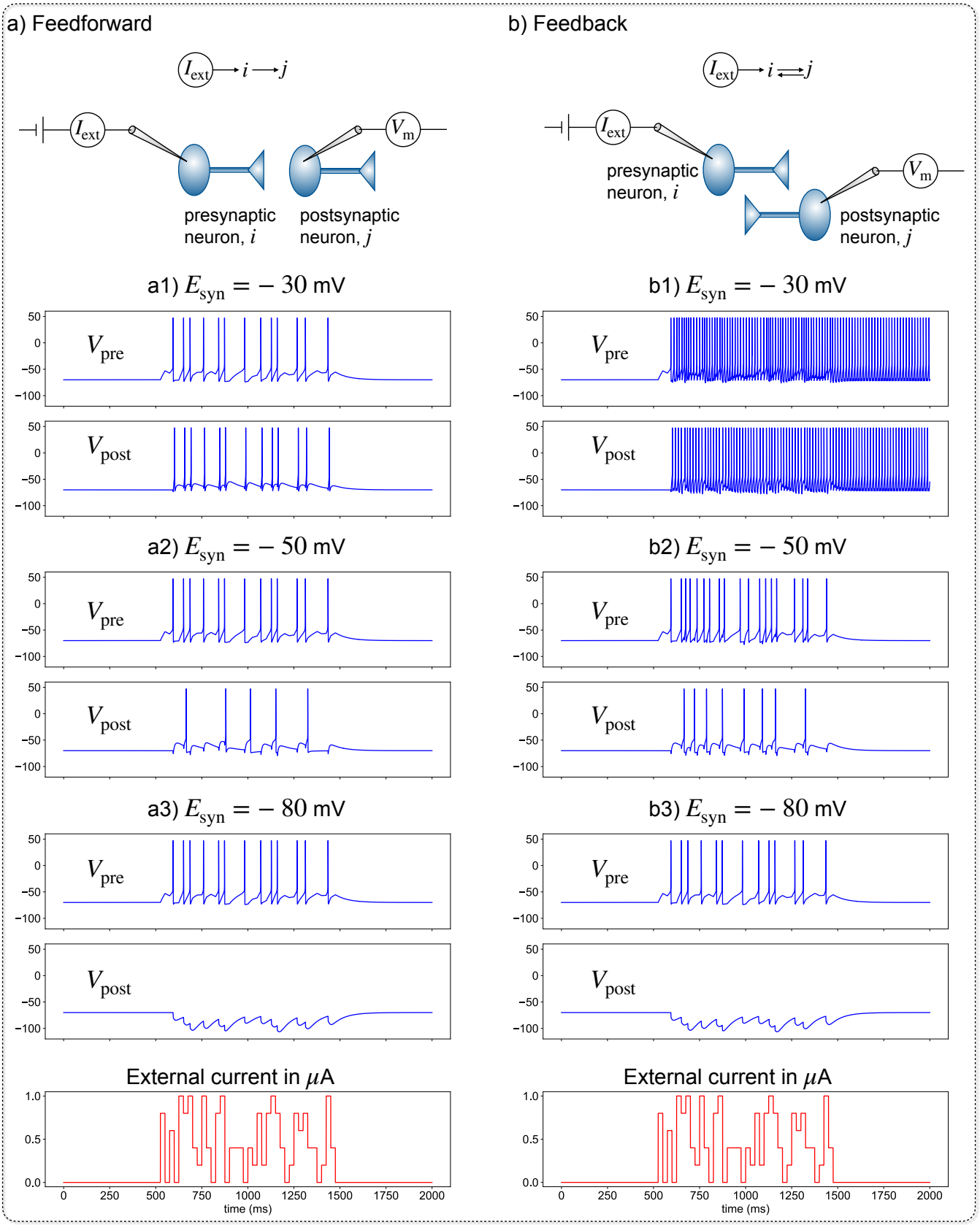

Figure 2: Model two-neuron microcircuits considered in this study: a) Feedforward circuit with neuronal dynamics described by Eq. 4 and Eq. 8; b) Feedback circuit described by Eq. 11 and Eq. 8. For the current pulse shown at the bottom, excitatory dynamics are described by synaptic activity shown in panels a1 and b1, while inhibitory dynamics are shown in panels a3 and b3.

where I_{Na} and I_{K} represent the sodium and potassium currents that underlie the action potential. Although the classical Hodgkin–Huxley formalism primarily focuses on Na^+ and K^+ currents, calcium ions also play a crucial role in neuronal signaling. Mammalian neurons express multiple types of voltage-gated Ca^{2+} channels that permit Ca^{2+} entry, hence, serving as a potent intracellular messenger. Their direct contribution to action-potential upstroke is typically small compared to Na^+ because Ca^{2+} channels activate more slowly. However, during the peak of the action potential, the depolarization is sufficient to open these channels, allowing Ca^{2+} influx. This influx can in turn activate large-conductance Ca^{2+}-activated potassium channels (BK channels or big potassium channels), which drive substantial K^+ efflux, overpowering the Ca^{2+} entry and accelerating membrane repolarization [26].

These are expressed in terms of the maximal conductances ($\overline{g}$), activation variables (m for Na^+ and n for K^+), and the Na^+ inactivation variable (h):

$$I_{\mathrm{Na},i}(t) = \overline{g}_{\mathrm{Na},i}\, m^3 h \left(V_i(t) - E_{\mathrm{Na}}\right), \tag{5}$$

$$I_{\mathrm{K},i}(t) = \overline{g}_{\mathrm{K},i}\, n^4 \left(V_i(t) - E_{\mathrm{K}}\right). \tag{6}$$

In standard neurophysiological electrode recordings, the neuron effectively acts as a single branch of an electrical circuit. The conductance parameters $\overline{g}$ represent the ease with which ions (e.g., Ca^{2+}, Na^+, and K^+) flow across the membrane, functioning analogously to variable conductances in an electrical network. The direction of ionic flow is determined by the reversal potentials E_{Na} and E_{K}; when $V_i(t)$ equals these values, there is no net flux of the respective ions. The leak current represents passive ionic fluxes not explicitly captured by the sodium or potassium channels, effectively accounting for background contributions such as chloride flow [24]:

$$I_{\mathrm{leak},i}(t) = \overline{g}_{\mathrm{leak},i} \left(V_i(t) - E_{\mathrm{leak}}\right). \tag{7}$$

We model two types of microcircuit motifs, as illustrated in Figure 2. For both cases, the spike-driven dynamics of the postsynaptic membrane potential are described by a modified Hodgkin–Huxley model (HHM) without external current:

$$C_m \frac{dV_j}{dt} = -I_{\mathrm{Na},j}(t) - I_{\mathrm{K},j}(t) - I_{\mathrm{leak},j}(t) - I_{\mathrm{syn},i\to j}(t), \tag{8}$$

where the notation $a \to b$ indicates that b is the postsynaptic neuron receiving input from the presynaptic neuron a. The synaptic current is defined as [27]

$$I_{\mathrm{syn},i\to j}(t) = \overline{g}_{\mathrm{syn},i\to j}\, r_i(t) \left(V_j(t) - E_{\mathrm{syn}}\right), \tag{9}$$

where $r_i(t)$ is the fraction of bound postsynaptic receptors. Initially, $r_i(0) = 0$, and its dynamics follow [22, 27]

$$\frac{dr_i}{dt} = \left(\frac{1}{\tau_r} - \frac{1}{\tau_d}\right) \cdot \frac{1 - r_i}{1 + \exp\left(-V_i(t) + V_0\right)} - \frac{r_i(t)}{\tau_d}, \tag{10}$$

with τ_r and τ_d denoting the rise and decay time constants, respectively. The values of τ_r, τ_d, and V_0, taken from [22], are listed in Table 1.

The difference in the dynamics of both motifs arises from the presynaptic response. For the type-a motif resulting in feedforward communication (see Figure 2 a), the presynaptic potential follows Eq. 4. For the type-b motif (see Figure 2 b), the potential for the presynaptic neuron also includes the synaptic current term as a feedback

$$C_m \frac{dV_i}{dt} = I_{\mathrm{ext}}(t) - I_{\mathrm{Na},i}(t) - I_{\mathrm{K},i}(t) - I_{\mathrm{leak},i}(t) - I_{\mathrm{syn},j\to i}(t). \tag{11}$$

For an excitatory synapse, $I_{\mathrm{syn},j\to i}(t)$ can result in perpetual (or recurrent) spikes as shown in Figure 2 (see b1).

The rate equations for the gating variables, common to both pre- and postsynaptic neurons and adopted from Ref. [22], are given as follows. For the sodium activation variable $m(t)$

$$\frac{dm}{dt} = \alpha_m(V)\big(1 - m(t)\big) - \beta_m(V)\, m(t), \tag{12}$$

with

$$\alpha_m(V) = \frac{-0.32\,(V - V_T - 13)}{\exp\left(-\frac{V - V_T - 13}{4}\right) - 1};\ \beta_m(V) = \frac{0.28\,(V - V_T - 40)}{\exp\left(\frac{V - V_T - 40}{5}\right) - 1}. \tag{13}$$

For the sodium inactivation variable $h(t)$, we have

$$\frac{dh}{dt} = \alpha_h(V)\big(1 - h(t)\big) - \beta_h(V)\, h(t), \tag{14}$$

with

$$\alpha_h(V) = 0.128\ \exp\left(-\frac{V - V_T - 17}{18}\right);\ \beta_h(V) = \frac{4}{\exp\left(-\frac{V - V_T - 40}{5}\right) + 1}. \tag{15}$$

Lastly, the potassium activation variable $n(t)$ follows

$$\frac{dn}{dt} = \alpha_n(V)\big(1 - n(t)\big) - \beta_n(V)\, n(t), \tag{16}$$

with

$$\alpha_n(V) = \frac{-0.032\,(V - V_T - 15)}{\exp\left(-\frac{V - V_T - 15}{5}\right) - 1};\ \beta_n(V) = 0.5\ \exp\left(-\frac{V - V_T - 10}{40}\right). \tag{17}$$

The parameters listed in Table 1 are adopted from Ref. [22]. In that study, fast-spiking (FS) cortical neurons were modeled within the Hodgkin–Huxley framework using only I_{Na} and I_{K} currents, consistent with our approach. FS neurons are a subtype of cortical interneurons characterized by rapid repolarization, brief action potentials, and the ability to generate high-frequency trains of spikes upon activation [23, 28]. Accordingly, the equations and parameter values employed here correspond to the FS cells of the rat somatosensory cortex.

In our simulations, V_{rest} (i.e., $V(0)$ of pre- and post-synaptic neurons) at the initial time ($t = 0$) was set to -70 mV. The driving force of the synaptic current is given by the difference between $V(t)$ and E_{syn}. If E_{syn} exceeds the membrane potential, the response is excitatory (Figure 1a); conversely, if E_{syn} lies below the membrane potential, the postsynaptic response is inhibitory (Figure 1b). The maximal synaptic conductance $\overline{g}_{\mathrm{syn}}$ was set to 0.2 mS/cm^2, consistent with the previous study [22]. The total simulation time was 2000 ms (2 s), with an external current $I_{\mathrm{ext}}(t)$ applied between 500 and 1500 ms. During this interval, for every 25 ms window, a constant current value was randomly selected from the set $\{0.0, 0.2, 0.4, 0.6, 0.8, 1.0\}$ μA. The effect of varying current-pulse magnitudes is analyzed in Figure 3.

In clinical neurophysiology, electrical signals must be sampled at sufficiently high temporal resolution to resolve action-potential

waveforms. Typical spike durations range from 10^{-1} to 10^{-2} ms, amounting to sampling rates on the order of 10^5 samples per second. Accordingly, a 1-s recording epoch requires approximately 10^5 data points, corresponding to a time step of about 0.01 ms [29]. To integrate Eq. 1, we employed the `odeint` solver from the `scipy` library [30], which wraps the well-established *Livermore Solver for Ordinary Differential Equations with Automatic method switching* (LSODA) algorithm [31]. LSODA automatically switches between non-stiff and stiff integration methods and adaptively adjusts the internal step size to preserve numerical stability and accuracy. The tolerances `rtol` and `atol` were chosen to control the global error of the solution and to ensure that the integration dynamically accounts for rapid variations in the solution.

Table 1: Parameters employed in solving Eqs.(4, 8, and 11), which describe models of fast-spiking cortical neurons adapted from Ref.[22].

Model parameter	Unit	Values
C_m	μF/cm^2	1
E_{K}	mV	-90.0
E_{Na}	mV	50.0
E_{leak}	mV	-70.0
g_{K}	mS/cm^2	10.0
g_{Na}	mS/cm^2	56.0
g_{leak}	mS/cm^2	0.015
V_T	mV	-56.2
τ_r	msec	0.5
τ_d	msec	8
V_0	mV	-20

Microcircuit motifs form the backbone of neural networks. Two fundamental types are the feedforward and feedback motifs (see Figure 2). In a feedforward motif, neurons are connected in series such that information flows in a single direction [32]. In contrast, in a feedback motif, the presynaptic neuron also receives input from its postsynaptic partner, in addition to external current, which can lead to sustained reciprocal activation. Motifs can be excitatory or inhibitory depending on the neurotransmitter released at the synapse. In modeling, this effect is captured implicitly through the parameters $\overline{g}_{\mathrm{syn}}$ and E_{syn}.

In addition to feedforward and feedback, other types of motifs are also present in neural networks. One example is lateral excitation or inhibition, where signaling is not transmitted through direct point-to-point synaptic contacts but rather via the diffusion of neurotransmitters, monoamines, or neuromodulators within a population of axons [32, 33]. Another example is disinhibition, a motif in which inhibition is transiently and selectively blocked, thereby producing net excitation [34].

In this study, we analyzed feedforward and feedback motifs under both excitatory and inhibitory regimes by observing the electrical activity of two coupled neurons (Figure 2). In the feedforward case, when an external current is applied to the presynaptic neuron and the synaptic reversal potential is set to $E_{\mathrm{syn}} = -30$ mV, the postsynaptic neuron is strongly excited. This occurs because the V_{rest} in our simulations is -70 mV, creating a large driving force for the synaptic current. Such values of E_{syn} are characteristic of excitatory neurotransmitters such as glu. Under these conditions, the presynaptic and postsynaptic neurons exhibit similar spiking patterns (Figure 2a1). A comparable effect is observed in the feedback (recurrent) motif, where excitation of the presynaptic neuron drives the postsynaptic neuron, producing matched spike trains (Figure 2b1). When E_{syn} is reduced to -50 mV in the feedforward motif, the postsynaptic neuron generates fewer spikes than the presynaptic neuron (Figure 2a2). This reduction reflects the weaker driving force at the lower E_{syn}. A similar decrease in postsynaptic spiking is observed in the feedback motif (Figure 2b2). However, comparing presynaptic activity across motifs reveals higher spike counts in the feedback case. This is because postsynaptic excitation in the feedback loop reactivates the presynaptic neuron, thereby amplifying its firing. At $E_{\mathrm{syn}} = -80$ mV, which is lower than the resting membrane potential, the postsynaptic neuron is inhibited (Figures 2a3,b3). When $E_{\mathrm{syn}} \lessapprox -70$ mV, the regime corresponds to shunting inhibition, where excitatory input is counteracted by proximal inhibitory input, causing depolarizing current to leak out before reaching the soma. Further lowering of E_{syn} produces stronger hyperpolarization ($V_m \ll E_{\mathrm{syn}}$), a hallmark of inhibitory synaptic transmission (Figure 1).

Table 2: Classification scores for various machine learning methods for predicting the labels of two microcircuit motifs using spike counts of postsynaptic action potential from 1000 simulations. The total simulation time was 2000 ms, and the external current was applied to the presynaptic neuron from 500 ms to 1500 ms, during which postsynaptic spikes were counted and binned. All simulations were done for $\overline{g}_{\mathrm{syn}} = 0.2$ mS/cm^2 and $E_{\mathrm{syn}} = -50$ mV.

N_{bin}	KNN	SGD	RF	SVC	GB
1	0.569	0.715	0.718	0.718	0.718
2	0.595	0.688	0.726	0.716	0.726
5	0.686	0.680	0.711	0.722	0.732
10	0.652	0.686	0.712	0.720	0.726
20	0.621	0.648	0.707	0.723	0.734
40	0.563	0.657	0.680	0.702	0.722

3 Classification of Microcircuit Motifs using Supervised Machine Learning

From the current-pulse simulations of both microcircuit motifs, we extracted postsynaptic spike counts and organized them into feature vectors by binning over different time intervals (N_{bin}). For $N_{\mathrm{bin}} = 1$, the feature vector corresponds to the total spike count during the 500–1500 ms window in which the external current was applied. For $N_{\mathrm{bin}} = 2, 5, 10, 20, 40$, spikes were summed over bin widths of 500, 200, 100, 50, and 25 ms, respectively. These binned spike counts serve as input features, while the motif labels (0 or 1) are the targets to train supervised machine learning models. The classifiers considered in this study are: K-nearest neighbors (KNN, $k = 5$), stochastic gradient descent (SGD), random forest (RF), support vector classifier (SVC), and gradient boosting (GB). All ML calculations were performed using the `scikit-learn` library [35].

For an initial assessment of the performance of various classifiers, we generated a dataset based on simulations with fixed values $\overline{g}_{\text{syn}} = 0.2$ mS/cm^2, $E_{\text{syn}} = -50$ mV, and external current pulses of constant amplitude applied in 25 ms intervals during the 500–1500 ms window of a total 2000 ms simulation. Current amplitudes were randomly selected from the range $[0,\ 1]$ μA in steps of 0.2 μA. For each microcircuit motif, 1000 simulations were performed by numerically solving Eqs. (4, 8, 11), with initial membrane potentials (i.e., V_{rest}) set to $V(0) = -70$ mV. This procedure yielded 2000 data points in total, each consisting of a feature vector (binned spike counts) and an associated target label (0 or 1).

Overall classification accuracy is defined as the fraction of correctly predicted labels over the total number of predictions. In terms of the confusion matrix entries,

$$\text{Accuracy} = \frac{\text{TP} + \text{TN}}{\text{TP} + \text{TN} + \text{FP} + \text{FN}}, \tag{18}$$

where TP, TN, FP, and FN denote the number of true positives, true negatives, false positives, and false negatives, respectively. All four terms are summed over both classes. The scores reported correspond to the mean accuracies obtained from 5-fold cross-validation. In this procedure, the dataset is partitioned into five subsets of equal size (20% each). Each subset is used once as the test set, while the remaining 80% of the data was used for training. With sufficient training data, the expected minimum classification score is 0.5, which corresponds to random guessing of labels. The upper bound is 1.0, representing perfect classification on the test set. Scores below 0.5 may arise when training sets are minimal, reflecting high variance in model performance due to sampling bias.

Table 2 reports the classification accuracies (as defined in Eq. 18) for all five models considered in this study, using feature vectors constructed from spike counts binned at different temporal resolutions. For training, 80% of the 2000 data points (1000 current-pulse simulations per motif) were used with 5-fold cross-validation. We focused on $E_{\text{syn}} = -50$ mV (with $\overline{g}_{\text{syn}} = 0.2$ mS/cm^2), which represents an intermediate regime where the synapse is neither strongly excitatory ($E_{\text{syn}} \gg V(0)$) nor strongly inhibitory ($E_{\text{syn}} \ll V(0)$). In general, ensemble methods such as RF and GB outperform simpler models like KNN and SGD, while SVC (a kernel-based method) also shows competitive performance. Cross-validated accuracies in the range of 0.65–0.73 (for $N_{\text{bin}} = 10$ in Table 2) across classifiers indicate that spike-binned features provide moderate discriminative power. Performance consistently exceeded the chance level of 0.5, confirming that motif types can be distinguished from spike statistics, though with substantial feature overlap that prevents near-perfect classification. An interesting trend observed across all classifiers is that the maximum accuracy was not obtained at the highest number of bins ($N_{\text{bin}} = 40$). This suggests that increasing the temporal partitioning of spike counts does not always add useful information, and at finer bin widths, the classifiers may instead be affected by noise. The highest accuracy of 0.734 was achieved by GB at $N_{\text{bin}} = 20$, showing that although the motifs are distinguishable, the overlap of spike-based features still limits classification performance to well below perfect accuracy.

To examine how classification performance improves with training set size, we repeated the ML calculations using different numbers of data points. Table 3 summarizes the variation in accuracy for classifying microcircuit motifs as the number of pulses (N_{pulses}) increases. Each dataset contains $2N_{\text{pulses}}$ data points, of which 80% are used for training and 20% for testing under 5-fold cross-validation. For smaller training sets, some models occasionally report higher scores, but these results are accompanied by large variances due to sampling bias. Thus, with different selections of training data of the same size, the observed accuracies can fluctuate considerably. For large training sets, GB achieves the highest accuracies of 0.720 and 0.734 for $N_{\text{pulses}} = 500$ and 1000, respectively. For GB with $N_{\text{bin}} = 20$, we extended the training to a larger dataset of 4000 points and obtained an improved accuracy of 0.749. These results suggest that, as long as the overlapping fraction of features between the two classes is not uniformly distributed, additional training data can enhance the performance of ML classifiers.

Table 3: Classification scores for various machine learning methods for predicting the labels of two microcircuit motifs using spike counts of postsynaptic action potential. For each microcircuit motif, N_{pulses} simulations were performed with random current pulses. The total simulation time was 2000 ms, and the external current was applied to the presynaptic neuron from 500 ms to 1500 ms, during which spikes were counted and binned for a time interval of 50 ms (i.e. $N_{\text{bin}} = 20$). All simulations were done for $\overline{g}_{\text{syn}} = 0.2$ mS/cm^2 and $E_{\text{syn}} = -50$ mV.

N_{pulses}	KNN	SGD	RF	SVC	GB
100	0.565	0.655	0.610	0.640	0.660
200	0.550	0.565	0.570	0.605	0.590
300	0.550	0.647	0.655	0.683	0.718
400	0.575	0.635	0.661	0.679	0.702
500	0.614	0.649	0.686	0.717	0.720
1000	0.621	0.648	0.707	0.723	0.734

Figure 3 shows the variation of GB classification accuracy across the parameter space defined by E_{syn} and $\overline{g}_{\text{syn}}$. We sampled 11 values for each parameter, resulting in 121 combinations. For each combination, 100 random current pulses were applied over a duration of 1 s, with pulse widths of 25 ms and amplitudes drawn from the range 0.0–1.0 μA in steps of 0.2 μA (top-left panel of Figure 3). Similar calculations were repeated for stronger input ranges: 0.2–1.0 μA, 0.4–1.0 μA, and 0.6–1.0 μA. In the intermediate conductance range ($\overline{g}_{\text{syn}} = 0.4$–$0.6$), an excitatory trend emerges for $E_{\text{syn}} > -50$ mV. For smaller conductances, the classification score often collapses to ~0.5, reflecting inhibition in both motifs—even when E_{syn} takes moderately depolarizing values (e.g., −45 mV at $\overline{g}_{\text{syn}} = 0.1$). For stronger conductances ($\overline{g}_{\text{syn}} > 0.5$), the trend in classification score is non-monotonic. Here, $E_{\text{syn}} < -65$ mV reliably indicates inhibition, and $E_{\text{syn}} > -40$ mV indicates excitation, while intermediate values yield scores in the range 0.6–0.9, particularly under stronger current pulses.

4 Conclusions

The difference between the synaptic reversal potential and the membrane potential determines the postsynaptic response to a

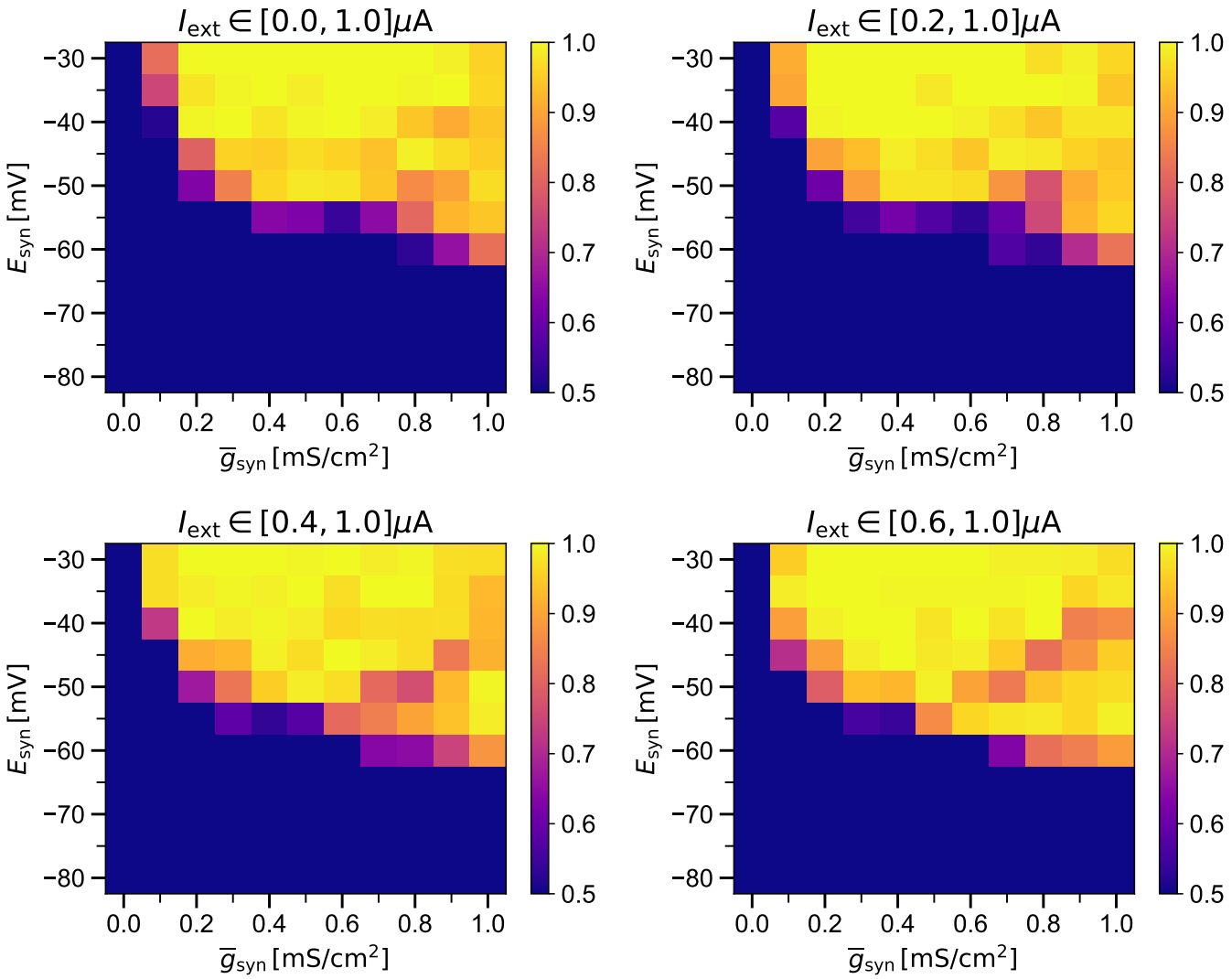

Figure 3: Accuracy, as defined in Eq. 18, for a GB-classifier to identify the microcircuit motifs (see Figure 2) using binned postsynaptic spike counts (total duration: 1000 ms, bin width: 50 ms). Average classification scores are reported as heatmaps for each combination of $\overline{g}_{syn}$ and E_{syn} parameters using 5-fold cross-validation of data obtained from simulations of each microcircuit motif using 100 random current pulses of magnitudes specified above the heatmaps.

synaptic current. Under certain conditions, such as brain development, epilepsy, or schizophrenia, the classical distinction between excitatory and inhibitory synapses can be blurred. In this work, we constructed a map in the parameter space spanned by E_{syn} and $\overline{g}_{syn}$ to identify regions associated with distinct synaptic regimes. To this end, we simulated Hodgkin–Huxley-type equations for prototypical two-neuron microcircuit motifs under current-pulse stimulation. The binned spike counts of postsynaptic neurons were then used as features to classify the motifs with various supervised ML models. While the total spike count over the stimulus duration (1 s) provided a useful measure of average firing rate and interpretability, some methods (e.g., RF, SVC, GB) showed improved performance when using binned spike trains that capture temporal trends in firing rates. However, excessively fine binning introduced noise, which degraded classifier performance in a method-dependent manner.

This study highlights parameter regions in which excitatory (classification score ~ 1), inhibitory (score ~ 0.5), and ambiguous synaptic behaviors can be identified. The purpose was not to classify networks at every level of excitation or inhibition, but rather to chart distinguishable versus indistinguishable regimes in a data-driven fashion. A key challenge for machine learning methods is to improve classification performance in these ambiguous intermediate regions, where synaptic polarity is diminished and the separation between regimes is blurred.

Several limitations remain. First, the model is restricted to two fast-spiking cortical neurons, which cannot fully capture the simultaneous dynamics of larger, heterogeneous populations. Second, only feedforward and feedback motifs were considered, whereas real neural networks also include lateral excitation, inhibition, and disinhibition motifs. Extending the framework to such motifs and to heterogeneous networks would add biological realism and provide a stronger basis for mapping synaptic alterations in complex circuits. Overall, this work represents a step toward quantitatively mapping synaptic regimes in simplified microcircuits, with potential applications towards understanding brain networks where excitation and inhibition are not strictly dichotomous.

Acknowledgments

We acknowledge the support of the Department of Atomic Energy, Government of India, under Project Identification No. RTI 4007.

References

[1] Charles F Stevens. *Neurophysiology: A primer*. John Wiley & Sons Inc, 1966.
[2] Casey Henley. Postsynaptic Potentials, In: *Foundations of Neuroscience*, 2021.
[3] Anthony N Van Den Pol and Paul Q Trombley. Glutamate neurons in hypothalamus regulate excitatory transmission. *Neurosci. J.*, 13(7):2829–2836, 1993.
[4] Claudia Jatzke, Junryo Watanabe, and Lonnie P Wollmuth. Voltage and concentration dependence of Ca2+ permeability in recombinant glutamate receptor subtypes. *J. Physiol*, 538(1):25–39, 2002.
[5] Akihiko Kitamura, Hitoshi Ishibashi, Miho Watanabe, Yusuke Takatsuru, Malcolm Brodwick, and Junichi Nabekura. Sustained depolarizing shift of the GABA reversal potential by glutamate receptor activation in hippocampal neurons. *Neuroscience research*, 62(4):270–277, 2008.
[6] Valentin Stein and Roger A Nicoll. GABA generates excitement. *Neuron*, 37(3):375–378, 2003.
[7] Haram R Kim and Marco Martina. Bidirectional regulation of GABAA reversal potential in the adult brain: Physiological and pathological implications. *Life*, 14(1):143, 2024.
[8] Fang Han, Zhijie Wang, Ying Du, Xiaojuan Sun, and Bin Zhang. Robust synchronization of bursting Hodgkin–Huxley neuronal systems coupled by delayed chemical synapses. *International Journal of Non-Linear Mechanics*, 70:105–111, 2015.
[9] R Angus Silver. Neuronal arithmetic. *Nat. Rev. Neurosci.*, 11(7):474–489, 2010.
[10] Alain Destexhe, Zachary F Mainen, Terrence J Sejnowski, et al. Kinetic models of synaptic transmission. *Methods in Neuronal Modeling*, 2:1–25, 1998.
[11] Knut Kirmse. Non-linear GABAA receptors promote synaptic inhibition in developing neurons: Commentary on Lodge et al.(2021) Sparsification of AP firing in adult-born hippocampal granule cells via voltage-dependent α5-GABAA receptors. Cell Rep 37: 109768. *Pflügers Archiv - European Journal of Physiology*, 474(2):181–183, 2022.
[12] Yehezkel Ben-Ari. Excitatory actions of GABA during development: the nature of the nurture. *NATURE REVIEWS* , 3(9):728–739, 2002.
[13] Carlijn Peerboom and Corette J Wierenga. The postnatal GABA shift: a developmental perspective. *Neuroscience & Biobehavioral Reviews*, 124:179–192, 2021.
[14] Kevin Staley and Roderic Smith. A new form of feedback at the GABAA receptor. *Nature neuroscience*, 4(7):674–676, 2001.
[15] Kartik Ramamoorthi and Yingxi Lin. The contribution of GABAergic dysfunction to neurodevelopmental disorders. *Trends Mol Med*, 17(8):452–462, 2011.
[16] Allan T Gulledge and Greg J Stuart. Excitatory actions of GABA in the cortex. *Neuron*, 37(2):299–309, 2003.
[17] Kai Kaila, Karri Lamsa, Sergei Smirnov, Tomi Taira, and Juha Voipio. Long-lasting GABA-mediated depolarization evoked by high-frequency stimulation in pyramidal neurons of rat hippocampal slice is attributable to a network-driven, bicarbonate-dependent K+ transient. *J. Neurosci*, 17(20):7662–7672, 1997.
[18] Jiaxin Yang, Xiong Yang, and Ke Tang. Interneuron development and dysfunction. *The FEBS Journal*, 289(8):2318–2336, 2022.
[19] Oscar Marín. Interneuron dysfunction in psychiatric disorders. *NATURE REVIEWS*, 13(2):107–120, 2012.
[20] Joseane Righes Marafiga, Mayara Vendramin Pasquetti, and Maria Elisa Calcagnotto. GABAergic interneurons in epilepsy: More than a simple change in inhibition. *Epilepsy & Behavior*, 121:106935, 2021.
[21] Yu-Qiang Liu, Fang Yu, Wan-Hong Liu, Xiao-Hua He, and Bi-Wen Peng. Dysfunction of hippocampal interneurons in epilepsy. *Neurosci Bull*, 30(6):985–998, 2014.
[22] Anastasia G Giannari and Alessandro Astolfi. Model design for networks of heterogeneous Hodgkin–Huxley neurons. *Neurocomputing*, 496:147–157, 2022.
[23] Martin Pospischil, Maria Toledo-Rodriguez, Cyril Monier, Zuzanna Piwkowska, Thierry Bal, Yves Frégnac, Henry Markram, and Alain Destexhe. Minimal Hodgkin–Huxley type models for different classes of cortical and thalamic neurons. *Biol Cybern*, 99(4):427–441, 2008.
[24] Alan L Hodgkin and Andrew F Huxley. A quantitative description of membrane current and its application to conduction and excitation in nerve. *J. Physiol*, 117(4):500, 1952.
[25] Alan Lloyd Hodgkin and Andrew Fielding Huxley. Propagation of electrical signals along giant nerve fibres. *Proc. Roy. Soc. London, Ser. B, Biol. Sci.*, 140(899):177–183, 1952.
[26] Bruce P Bean. The action potential in mammalian central neurons. *Nat. Rev. Neurosci.*, 8(6):451–465, 2007.
[27] A Destexhe, Z Mainen, and TJ Sejnowski. An Efficient method for computing synaptic conductances based on a kinetic model of receptor binding. *Neural computation*, 6:14–18, 1994.
[28] Vanessa F Descalzo, Lionel G Nowak, Joshua C Brumberg, David A McCormick, and Maria V Sanchez-Vives. Slow adaptation in fast-spiking neurons of visual cortex. *J Neurophysiol*, 93(2):1111–1118, 2005.
[29] E Karl. Essentials of clinical neurophysiology. *J. Clin. Neurosci.*, 6(3):272–274, 1999.
[30] Pauli Virtanen, Ralf Gommers, Travis E Oliphant, Matt Haberland, Tyler Reddy, David Cournapeau, Evgeni Burovski, Pearu Peterson, Warren Weckesser, Jonathan Bright, et al. SciPy 1.0: fundamental algorithms for scientific computing in Python. *Nature methods*, 17(3):261–272, 2020.
[31] Alan C Hindmarsh and Linda R Petzold. LSODAR, ordinary differential equation solver for stiff or non-stiff system with root-finding. 2005.
[32] Liqun Luo. Architectures of neuronal circuits. *Science*, 373(6559):eabg7285, 2021.
[33] Jason M Christie and Gary L Westbrook. Lateral excitation within the olfactory bulb. *J. Neurosci*, 26(8):2269–2277, 2006.
[34] Johannes J Letzkus, Steffen BE Wolff, and Andreas Lüthi. Disinhibition, a circuit mechanism for associative learning and memory. *Neuron*, 88(2):264–276, 2015.
[35] Fabian Pedregosa, Gaël Varoquaux, Alexandre Gramfort, Vincent Michel, Bertrand Thirion, Olivier Grisel, Mathieu Blondel, Peter Prettenhofer, Ron Weiss, Vincent Dubourg, et al. Scikit-learn: Machine learning in Python. *J. Mach. Learn. Res.*, 12:2825–2830, 2011.